Label-free quantitative chemical imaging and classification analysis of adipogenesis using mouse embryonic stem cells - Supporting information

Francesco Masia,[1,*] Adam Glen,[2] Phil Stephens,[2] Wolfgang Langbein,[1] and Paola Borri[3]

[1]*School of Physics and Astronomy, Cardiff University, The Parade, Cardiff, CF24 3AA, United Kingdom*

[2]*School of Dentistry, Cardiff University, University Hospital Wales, Heath Park, Cardiff, CF14 4XY, United Kingdom*

[3]*School of Biosciences, Cardiff University, Museum Avenue, Cardiff, CF10 3AX, United Kingdom*

Contents

S1. FSC^3 RESULTS

Fig. S1 shows the concentrations C_i and spectra obtained by the FSC^3 method applied to the analysed images. For illustration purposes, only two images are reported. The full data can be found in Ref. 1. In the algorithm, the hyperspectral data have been factorized into 5 chemical components $\mathcal{C}_i$. The components can be interpreted using their spectra and spatial distributions. The spectra of $\mathcal{C}_1$ and $\mathcal{C}_2$ show a rise at large wavenumbers and are mostly present outside the cells. They can be attributed to water which has a broad band in $\Im(\bar{\chi})$ covering (3200-3600) cm^{-1}. $\mathcal{C}_3$ has a similar spectrum as $\mathcal{C}_1$ and $\mathcal{C}_2$ with an additional band around 2800 cm^{-1}. This component can be interpreted as systematic fluctuation in

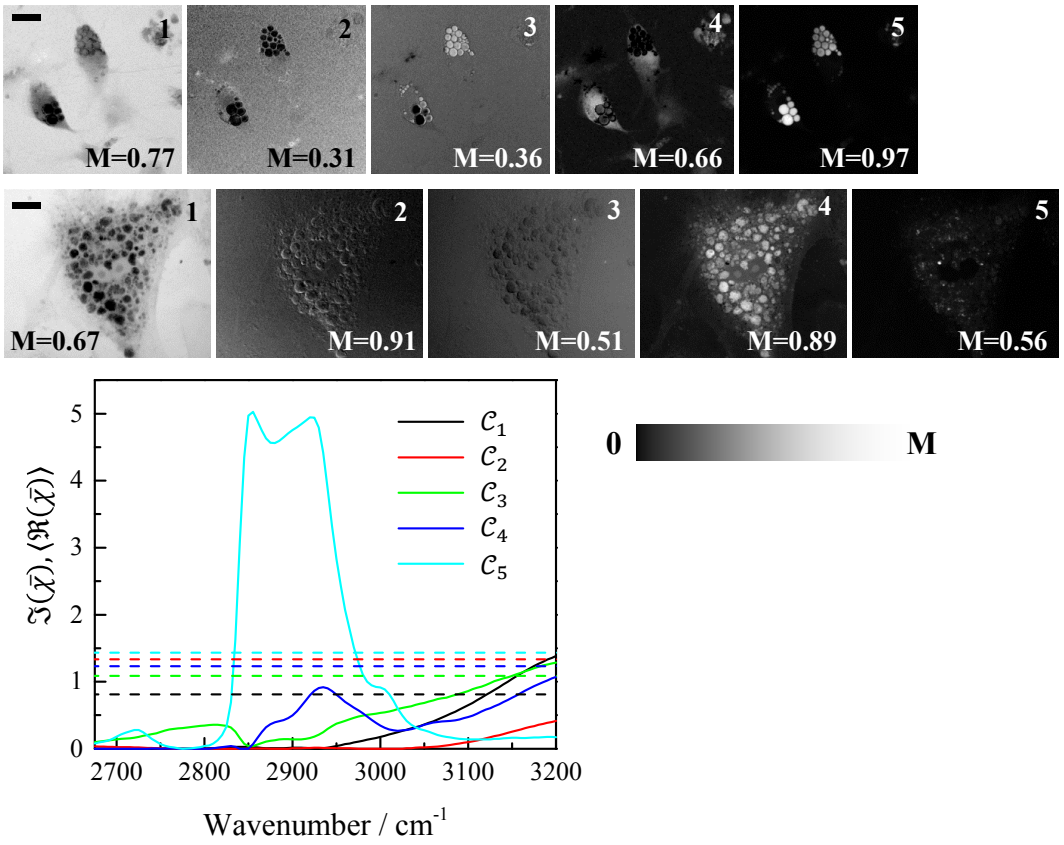

FIG. S1: Full results of the FSC^3 factorization for the cells shown in d) and e) of Fig. 1. The concentration maps $C_i(\mathbf{r})$ of the five components are shown using a grayscale from 0 to M as indicated. The scale bars indicate 20 μm. The graph shows the FSC^3 susceptibility spectra for the five components. The solid (dashed) lines refer to the imaginary (spectrally-averaged real) part, respectively.

the spectra of the water and lipid components as it is mostly concentrated in the water and in some lipid droplets in the pre-adipocytes. $\mathcal{C}_4$ is mostly localized in the cytosol of the pre-adipocytes and undifferentiated cells and in the vesicles of cells undergoing differentiation. The spectrum shows the typical resonance of proteins around 2960 cm^{-1} and is named $\mathcal{C}_\mathrm{P}$ (see spectrum measured in a pure albumin sample in Ref. 2). Finally, $\mathcal{C}_5$ has the typical spectral features of lipids (see spectra measured in a pure lipid model samples in Ref. 3) and is named $\mathcal{C}_\mathrm{L}$. Overlays of C_P and C_L for more cells than in Fig. 1 of the main text are presented in Fig. S2.

To show that the component spectra and concentrations from the FSC^3 analysis provide a truthful representation of the spectra after PCKK retrieval, specifically for the proteic

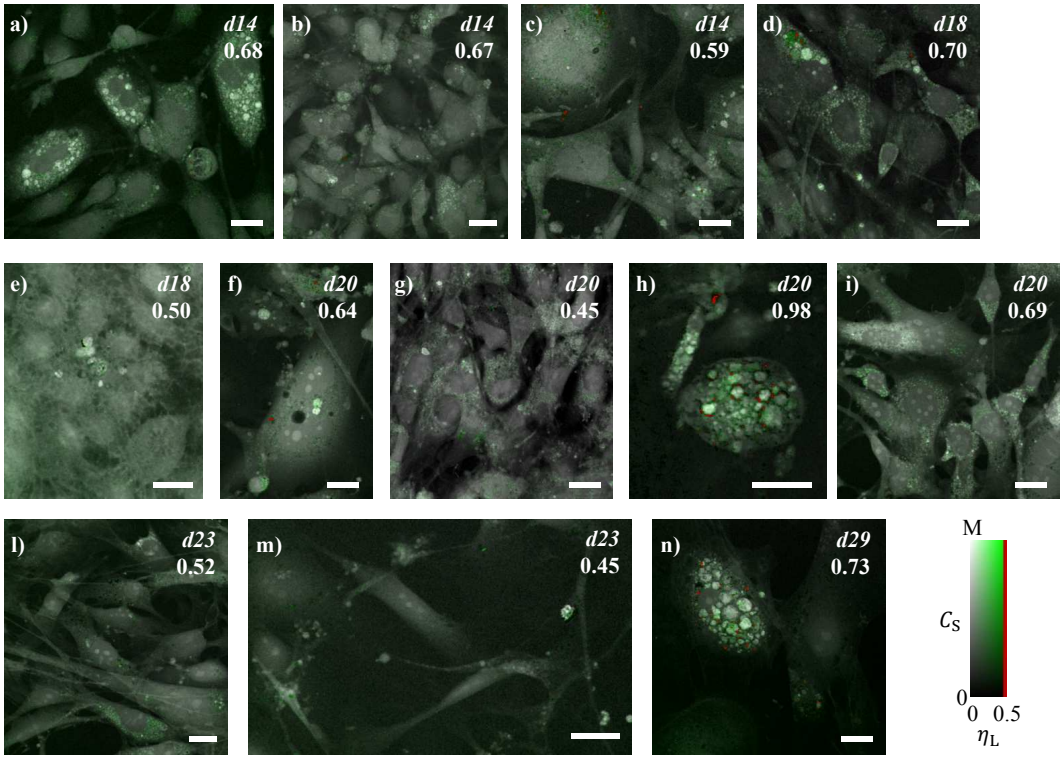

FIG. S2: Cells at different stages of differentiation imaged using hyperspectral CARS and FSC^3 factorization - more results as in Fig. 1 of the main text. Sum concentration C_S of protein and lipid $(0-M)$ as brightness, and the lipid fraction η_L $(0-0.5)$ as saturation of green, with $\eta_L > 0.5$ shown in red (see colour bar). The italic labels indicate the number of days in the differentiation medium before fixation. The roman labels indicate M. The scale bars indicate 20 μm.

glubules, we show in Fig. S3 the imaginary part of spectra averaged over a lipid droplet in a committed white pre-adipocyte (blue line), the cytosolic regions of a committed white pre-adipocyte (green line) and an undifferentiated cell (red line), and a globule (magenta line). The latter three spectra show similar features, with increasing concentration as given by the indicated factors, confirming the hypothesis that those regions, apart from the overall concentration, have a similar chemical composition. Notably, however, the concentration in the globules is about 4 times larger than in the cytosol of undifferentiated cells, and about 50% larger than in the cytosol of the pre-adipocytes.

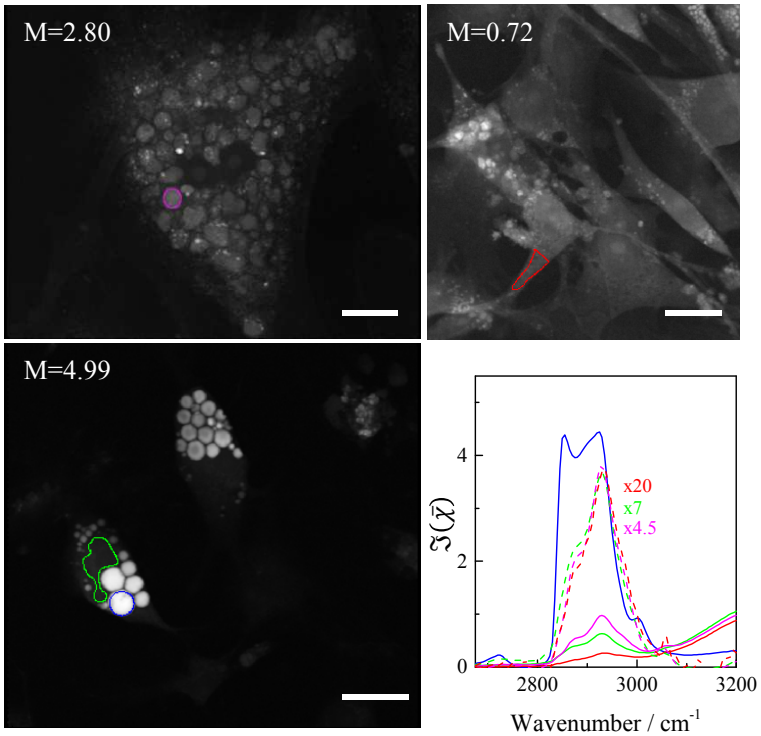

FIG. S3: Imaginary part of PCKK retrieved spectra averaged over different cell regions. The images show the spatial distribution of the imaginary part of the susceptibility at 2930 cm^{-1} on a grayscale from 0 to M as indicated. The scale bars indicate 20 μm. The coloured loops enclose the regions over which the spectra of corresponding colour shown in the graph as solid lines are averaged. The dashed lines in the graph show the spectra after removing the water contribution and scaling by the indicated factors.

S2. SPONTANEOUS RAMAN MEASUREMENTS

Fig. S4 shows the spontaneous Raman spectra in the fingerprint region acquired on lipid stored in white fat tissue from the abdomen of a mature mouse (black line), a 3t3l1-derived adipocytes (green line) and a mES cell derived pre-adipocyte (red line). The spectra have been a taken in a home-built Raman micro-spectrometer attached to the same microscope stand as the CARS set-up. The excitation beam was provided by a 50 mW continuous wave laser of 532 nm wavelength and coupled into the microscope by a Semrock LPD01-532RS-25 dichroic beamsplitter. The Raman scattering was collected in epi-direction, transmitted through the dichroic beamsplitter and a Semrock BLP01-532R-25 long-pass filter, spectrally dispersed by a Horiba Jobin-Yvon iHR550 imaging spectrometer with a 150 l/mm grating,

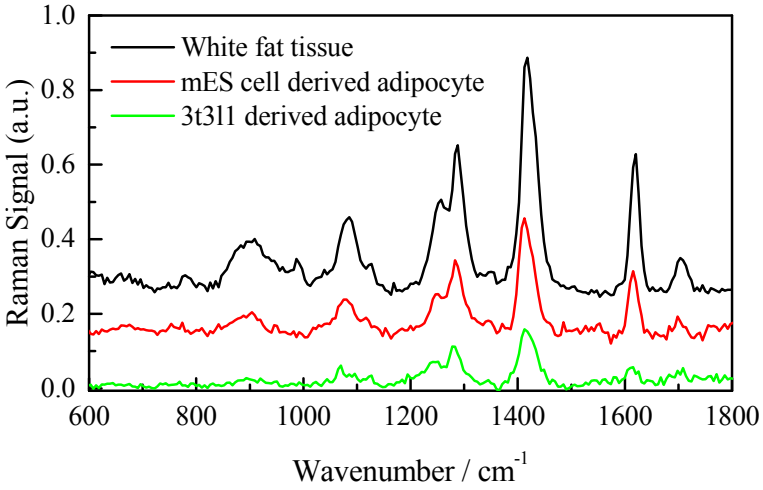

FIG. S4: Raman spectra acquired on lipid stored in white fat tissue from the abdomen of a mature mouse (black line), a 3t3l1-derived adipocytes (green line) and a mES cell derived pre-adipocyte (red line). Spectra are vertically offset for clarity.

and detected by a Andor Newton DU971N CCD camera, with 8 cm^{-1} resolution

The Raman spectrum in adipocytes was similar to that of white fat tissue, while spectral signatures typical of brown fat, i.e. two small Raman peaks between 1500 and 1600 cm^{-1} (see Ref.4), were absent.

S3. FLUORESCENCE - FSC^3 CORRELATION

WF images have been acquired on the same microscope as used for CARS. The illumination was provided by a metal-halide lamp (Prior Lumen200). A Semrock GFP-A-Basic-NTE filter cube was used to excite the sample over a wavelength range of 452 - 487 nm and to transmit the fluorescence over a range of 505 - 545 nm. A Hamamatsu ORCA 285 CCD camera was used to detect the fluorescence images with typical exposure times of 1-10 s. The objective used was the same as in the CARS investigation

At an early stage of differentiation (such as those in Fig. 1b) no significant immunostaining was observed (Fig. S5a), and the detected intensity is dominated by autofluorescence, as shown by comparison with unstained cells (Fig. S5b). The occurrence of localized fluorescence is most likely a staining artefact from unspecific immunostaining aggregation, sometime observed in peripheral regions of the cells (see also Fig. S7). Notably, this artefact was not observable in the FSC^3 components (see Fig. 1b). This shows the suitability of

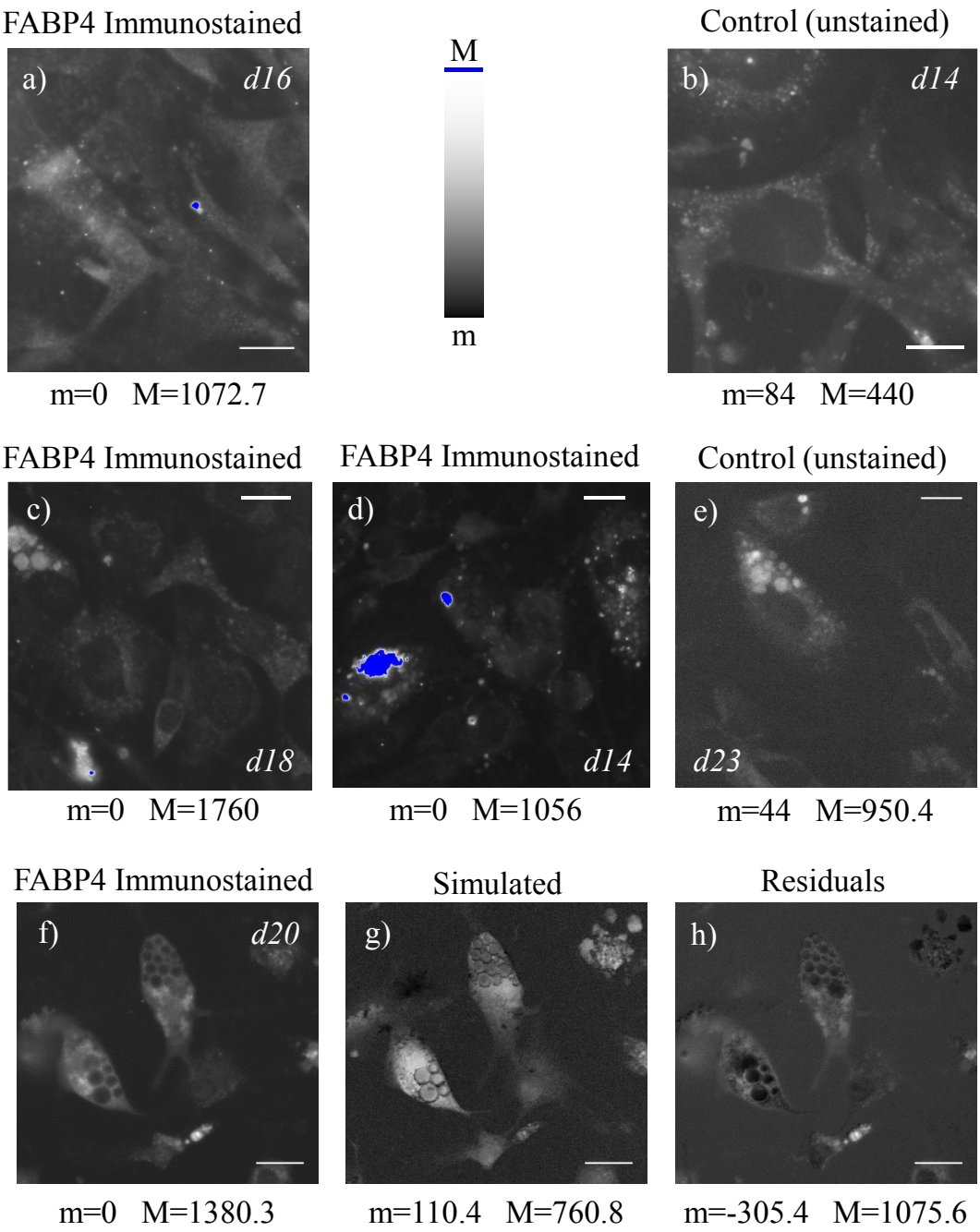

FIG. S5: Cells at different stages of differentiation investigated using WF microscopy. (a-f) Measured (I_{WF}) fluorescence intensity images in units of detected photoelectrons per second and pixel (equivalent pixel size on the sample $(180\,\mathrm{nm})^2$) for the field of view shown in Fig. 1b for (a), Fig. S2c for (b), Fig. S2d for (c), Fig. S2a for (d), Fig. 1c for (e), and Fig. 1e for (f). (a,c,d,f) are images on cells immunostained against the FABP4. (b,e) are autofluorescence measurements on control unstained cells. g) is the simulated intensity ($I_{\mathrm{WF}}^{\mathrm{FSC}}$) of f) with residuals (h). Linear grayscale from minimum m to maximum M as indicated. Values above M are shown in blue. The scale bars indicate $20\,\mu$m.

CARS for chemical analysis in a highly fluorescent environment, a distinct advantage over spontaneous Raman. It also shows that the FSC^3 results are not significantly affected by the immunostaining.

At intermediate stages of differentiation we observed a mixed scenario. In some cases, cells which show the presence of protein vesicles (see for example Fig. S5d for the WF, and the factorization results in Fig. S2a for the chemical assignment) also show high immunofluorescence. In some other cases, cells with protein vesicles (see for example the cell in the top left corner of Fig. S5c (WF) and Fig. S2d (FSC^3 results)) do not show a strong level of immunofluorescence, and the emission is rather dominated by autofluorescence of the protein vesicles (see for example the control unstained cell of Fig. S5e (WF) and Fig. 1c (FSC^3 results)).

In committed white pre-adipocytes as those shown in Fig. 1e, we observed that FABP4 immunostaining is present in the cytosol and absent inside the large lipid droplets (see Fig. S5f), as would be expected for this protein [5]. To identify correlations between the WF images and concentration maps of the FSC^3 components, and quantify the relative concentration of FABP4 immunostaining in the chemical components deduced by FSC^3 we expressed the fluorescence intensity I_{WF} as linear combination of the obtained FSC^3 concentrations C_i i.e. $I_{\mathrm{WF}}^{\mathrm{FSC}} = I\left(\sum a_i C_i\right)$. The coefficients a_i and I were obtained by minimizing the mean square deviation between $I_{\mathrm{WF}}^{\mathrm{FSC}}$ and I_{WF} with the constraint that $a_i \geq 0$ and $\sum a_i = 1$. [6] The resulting coefficients a_i represent the relative concentration of FABP4 immunostaining in the chemical component i, and the relative error in the fit $E = ||I_{\mathrm{WF}} - I_{\mathrm{WF}}^{\mathrm{FSC}}||/||I_{\mathrm{WF}}||$ gives a measure of the correlation between the FSC^3 components and the immunostaining. The best fit for the fluorescence in Fig. S5f is obtained for values of the coefficients associated to the protein and lipid components of 0.41 and 0.14, respectively, and with $E = 0.24$ i.e. only partial correlation. $I_{\mathrm{WF}}^{\mathrm{FSC}}$ resembles I_{WF} spatially (see Fig. S5g,h), with the majority of the contribution correlating with the protein channel. The weak correlation indicates that FABP4 expression is too low to generate a FSC^3 component that is solely attributed to this specific protein.

The fluoresence intensity measured between the different samples varies within a factor of two, which is not enough to unambiguously distinguish immunofluorescence from autofluorescence, as the latter can have similar level of fluctuations. Supporting evidence to the assignment that the fluorescence observed in pre-adipocytes is due to the dye can be

obtained by observing the difference of the spatial distribution between immunofluorescence and autofluorescence.

Indeed we observed that the autofluorescence in these cells had a more homogeneous distribution compared to the fluorescence associated with the FABP4 immunostaining. Fig. S6 shows fluorescence images of committed white pre-adipocytes immuno-stained with FABP4-FITC detected with three different emission filters. The red image is obtained by exciting at 562 ± 20 nm and detecting > 593 nm. The green image is obtained exciting at 469 ± 18 nm and detecting at 525 ± 20 nm. The blue image is obtained exciting at 370 ± 18 nm and detecting at 447 ± 30 nm. The three images have been acquired with 2 seconds integration time. The red and blue channels can be interpreted as autofluorescence as we do not expect excitation/emission of the dye for the combination of filters used. The green channel contains the immunofluorescence. The three channels show similar intensities but different distribution. The autofluorescence is more homogeneous in the cytosol while the immuno-fluorescence shows agglomerations. Similar distribution of the immuno-fluorescence was observed for other pre-adipocytes (see Fig. S5f), indicating that it is not dominated by autofluorescence. The fluorescence images often show very strong localized immunofluorescence. In Fig. S7, a strong emission is observed at the periphery of the cell membrane, which exceeds the immunofluorescence level observed in the pre-adipocytes. We believe that those localized emissions come from agglomerates of the antibody-dye complex which binds to unspecific structures of the cell membrane.

These results show that immunofluorescence can be observed in cells at an intermediate stage of differentiation suggesting that the FAB4 production is in parallel with the presence of large protein vesicles. However, the analysis is not conclusive as some immunostained cells with the protein vesicles show fluorescence intensities comparable to the autofluorescence observed in similar cells in control samples. The occurrence of staining artifacts from unspecific aggregation additionally hinders the use of FAB4 immunofluorescence as an unambiguous marker for differentiation into adipocytes.

S4. CLASSIFICATION

The features extracted from the concentration maps of the lipid and protein component are given in Table I. The autocorrelation length is defined as the distance where the angular-

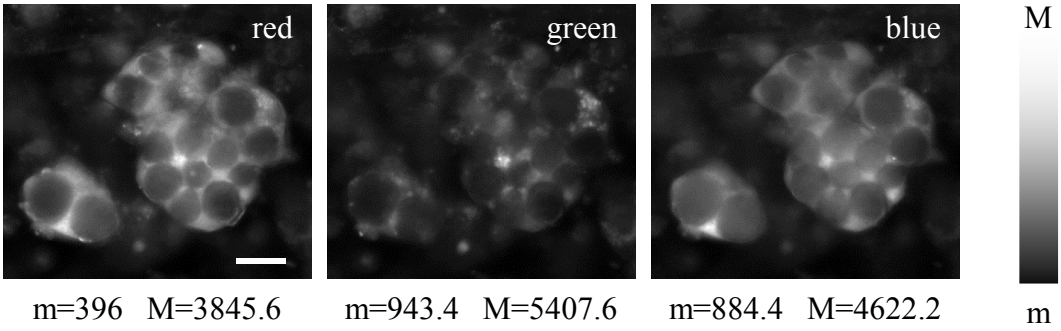

FIG. S6: Fluorescence intensity images measured for different filter cubes as discussed in the text. The grayscale is in units of detected photoelectrons per second and pixel (pixel size 180 nm × 180 nm), minimum m and maximum M values are indicated below each image. The scale bar indicates 20 μm.

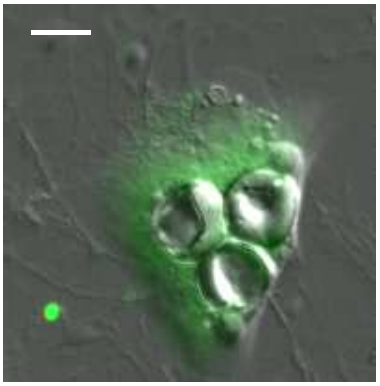

FIG. S7: Overlay of differential interference contrast (gray) and immunofluorescence (green) images of a committed white pre-adipocyte. Note the strong localized emission at the bottom left corner which exceeds the immunofluorescence level in the pre-adipocyte. The scale bar indicates 10 μm. The fluorescence scale is 145 to 1800 photoelectrons per second and pixel. The overlay has been generated by adding the scaled fluorescence image to the green channel of the DIC image.

index	Feature	PC_1	PC_2
1	Mean value of lipid concentration	-0.073	0.599
2	Standard deviation of lipid concentration	-0.063	0.588
3	Skewness of lipid concentration	0.329	-0.074
4	Kurtosis of lipid concentration	0.349	-0.122
5	Autocorrelation length of lipid concentration	0.401	0.007
6	Mean value of protein concentration	0.289	0.162
7	Standard deviation of protein concentration	0.301	0.373
8	Skewness of protein concentration	0.251	0.168
9	Kurtosis of protein concentration	0.273	0.058
10	Autocorrelation length of protein concentration	0.434	0.035
11	Crosscorrelation of lipid and protein concentrations	0.315	-0.276

TABLE I: Features extracted for cell classification, and corresponding coefficients of the first two principal components

averaged auto-correlation is equal to half the difference between its value at the origin and the average value over 75-100% of the maximum radius used (typically 65 μm).

S5. SUPPORT VECTOR MACHINE CLASSIFIER

For a specific number of clusters $2 \leq k \leq N_c - 1$, where N_c is the number of cells, we have determined all possible combinations of clusters determined by the HCA (see Fig. 3) which contain all cells. For example, for $k = 3$ we have two possible combinations. In the first one the clusters are formed by cells 19 and 20 (cluster 1), cell 33 (cluster 2), and all the other cells in the third cluster. The second combination sees the cells 19 and 20 in two different clusters and all the other cells (including now also cell 33) in the third cluster. For each combination we trained a binary linear support vector machine (SVM) model on each of the $k(k-1)/2$ cluster pairs. As predictors, we used the same PCs as in the HCA. The SVM model calculates the optimal decision boundary, a hyperplane in the PC space, which separates the clusters. The SVM defines a distance from the hyperplane, which is ± 1 for each object in a cluster pair without inter-cluster variation, where the sign identifies on

which side of the hyperplane the object is, each side corresponding to one of the two clusters. The hyperplane is defined by a vector in the N_{PC} - dimensional space of PCs plus a scalar offset, and has thus $N_{\mathrm{PC}}+1$ real parameters. For each cluster pair ι, the corresponding SVM results in a vector $\boldsymbol{\delta}^{(\iota)}$ of the distances of each of the $N^{(\iota)}$ objects in the cluster pair from the hyperplane. To judge the goodness of the separation of the cluster pair by the hyperplane, we use the square deviation

$$D^{(\iota)} = \eta \sum_{\kappa=1}^{N^{(\iota)}} \log\left(|\boldsymbol{\delta}_{\kappa}^{(\iota)}|\right)^2 ,$$

which provides a measure for the separation within the clusters relative to the separation between the clusters. The normalization η accounts for the number of free distances in the sum, given by $N_{\mathrm{f}}^{(\iota)} = N^{(\iota)} - N_{\mathrm{PC}} - 1$. If this number is larger than zero, we use $\eta = 1/N_{\mathrm{f}}^{(\iota)}$ to provide the mean error. Otherwise, there are at least as many parameters of the hyperplane as determining conditions and we would expect that the SVM provides distances of ± 1, so that the sum should be zero, and we use $\eta = 1$. If any object is classified by the SVM to the wrong cluster, i.e. the corresponding element of $\boldsymbol{\delta}^{(\iota)}$ has the wrong sign, the SVM cannot separate the clusters, and the FOM of the cluster combination is set to zero.

We define the figure of merit for the cluster combination as the inverse of the root mean square deviation, i.e. $\mathrm{FOM} = \sqrt{N_{\mathrm{vp}}/\sum_{\iota} D^{(\iota)}}$, where N_{vp} is the number of cluster pairs ι with $N_{\mathrm{f}}^{(\iota)} > 0$, which are expected to contribute to the error as discussed above.

S6. CLASSIFICATION RESULTS WITH $k = 22$

In Fig. 3 we show that the FOM has a second maximum at $k = 22$. Fig. S8 shows a scatter plot of the first two PCs where the symbol are colour coded according to the cluster configuration described by the blue dashed line in Fig. 3.

S7. DISTANCE-BASED CLUSTER VALIDATION INDEXES

Among the distance-based methods for cluster analysis validation, we calculated the Silhouette index [7] and the Kendall's tau as a function of the number of clusters. The Silhouette index measures how similar an object is to its own cluster compared to other clusters, averaged over the objects. It can vary from 1 to -1, with a good clustering configuration showing

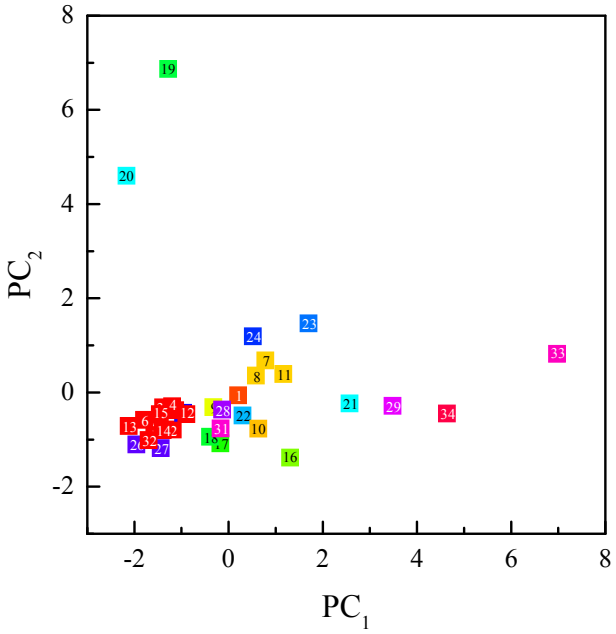

FIG. S8: Scatter plot of the first two PCs. The symbol colour reflects the affinity to a particular cluster corresponding to the configuration of maximum FOM when $k = 22$ clusters are considered.

a large Silhouette index. We found that the Silhouette is constant (~ 0.7) for a number of clusters less than 10, then it shows a dip and a monotonous increase (see Fig. S9), which is due to the fact that most clusters are formed by small number of objects. The Kendall's tau is a measurement of concordance between two set of measurements. For each pair of observations i, j, i.e. cells, we create a vector d which elements are given by the distance between them and a vector u which elements are either 0 or 1 if the observations are in the same cluster or not. We then compare the values of d and u for two pairs of observation i, j and $i\prime, j\prime$. If $u_{i,j} > u_{i\prime,j\prime}$ and $d_{i,j} > d_{i\prime,j\prime}$ or $u_{i,j} < u_{i\prime,j\prime}$ and $d_{i,j} < d_{i\prime,j\prime}$ the pair is concordant, otherwise is discordant. The Kendell's tau is the total number of concordant pairs minus the total number of discordant pairs normalized by the number of elements of d. The dependence of the Kendell's tau on the number of clusters in our HCA shows a maximum concordance for 10 clusters (see Fig. S10).

S8. HCA DEPENDENCE ON NUMBER OF PC CONSIDERED

As discussed above, we have extracted 11 features from the CARS images and we reduced the dimensionality by considering only the first 5 principal components (PC) of these features

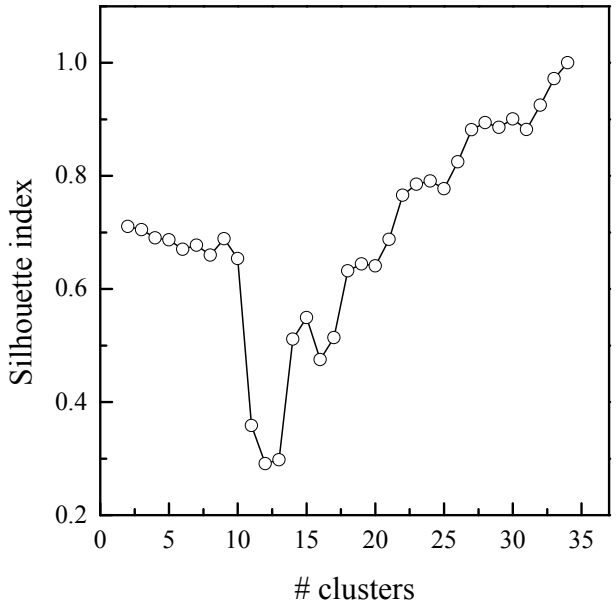

FIG. S9: Dependence of the Silhouette index on the number of clusters used in the HCA algorithm.

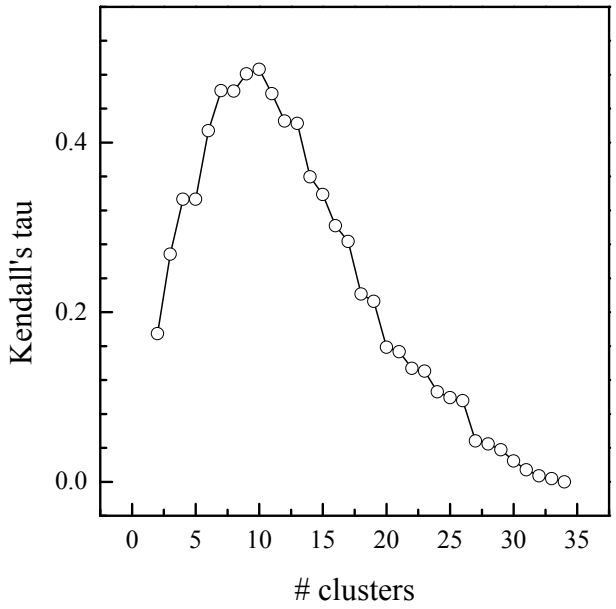

FIG. S10: Dependence of the Kendall's tau on the number of clusters used in the HCA algorithm.

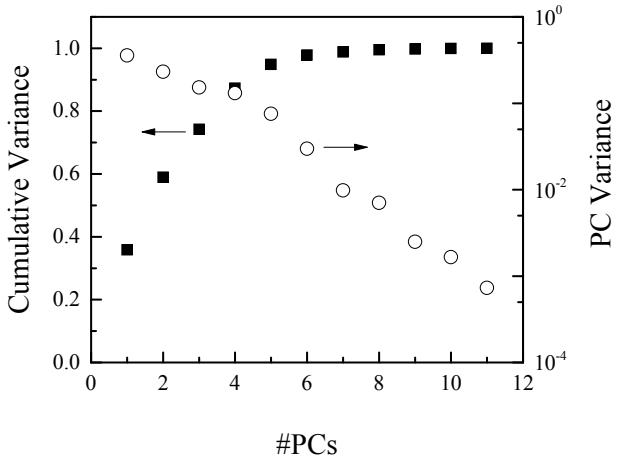

FIG. S11: Cumulative variance and PC variance as a function of the PC index.

over the cell ensemble to cluster the objects. The cumulative variance and the variance corresponding to each principal component are shown in Fig. S11

We have verified that increasing the number of PCs we obtain similar clustering, as we show in Fig. S12 and Fig. S13 resulting from using 6 or 7 PCs, respectively. The corresponding dendrograms are similar to what obtained considering 5 PCs, and the FOMs show an optimal number of clusters of 9. The general behaviour of the HCA is consistent with what shown in Fig. 3.

S9. CALCULATION OF PROTEIN DISTRIBUTION

To calculate the mean and standard deviation of the protein distribution around a lipid droplet, we applied the following method. First, we segmented the image of the FSC^3 component associated to lipid using the software CellProfiler to create a binary mask for each droplet, i.e. an image where the pixels in the region occupied by the lipid droplet have value 1 and zero otherwise. After an automatic segmentation with threshold concentration of 10% (to exclude a background with lipid content which cannot be clearly identified as a lipid droplet, such as the endoplasmatic reticulum and other membranes), we applied the declumping function of CP and subsequent manual editing to separate masks covering multiple droplets.

To obtain the central position and radius R of each LD, we extended the mask by 4 pixels ($0.72\,\mu$m) and fitted C_{L} inside the mask with a truncated Gaussian function distribution.

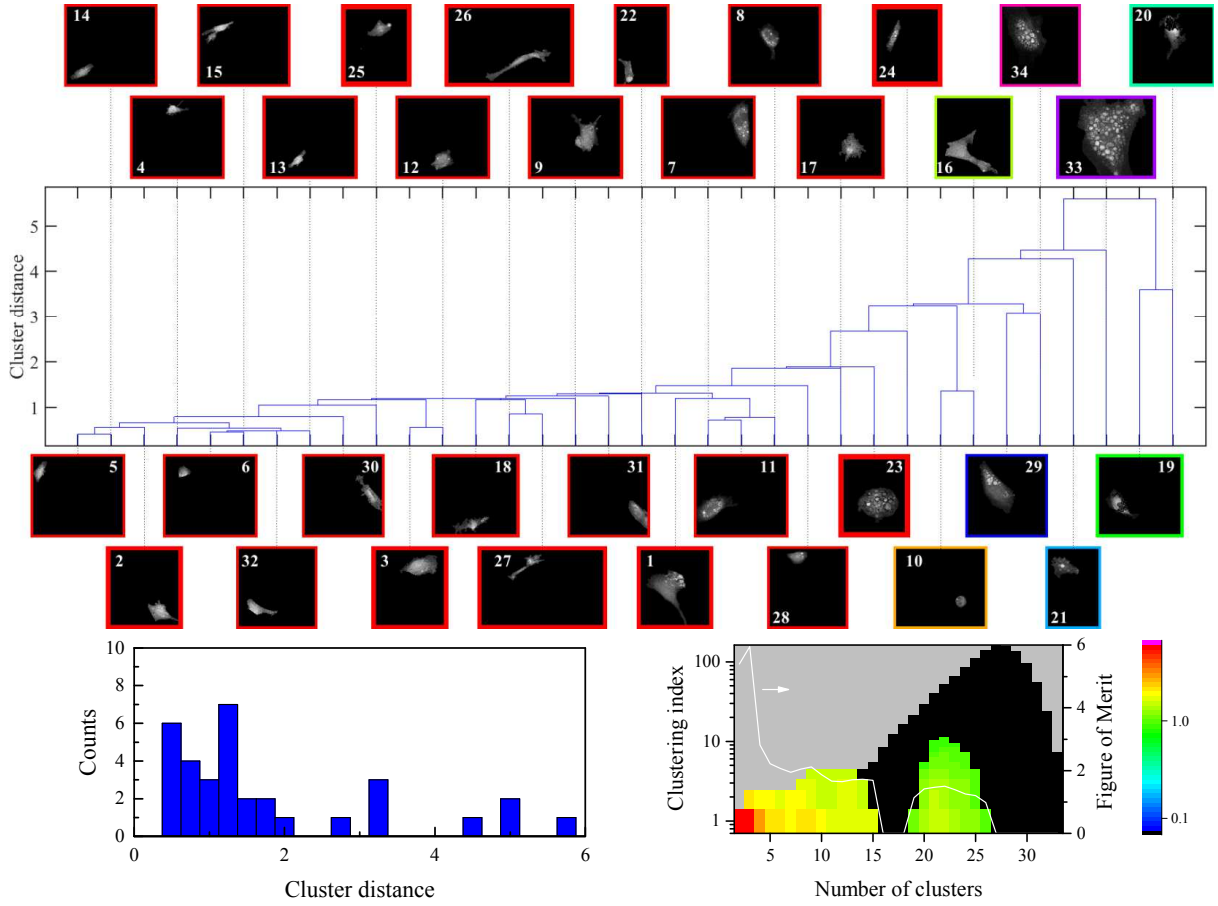

FIG. S12: Same as Fig. 3 when 6 PCs are included in the HCA.

Fig. S14 shows the method used to determine the centroid position of lipid droplet. The images show the lipid concentration in the areas indicated in Fig. 1(b,d). First, lipid droplets are segmented according to the method described above and a mask for each lipid droplet is generated. The red pixels identify the edge of the mask (see Fig. S14(a,c)). Second the mask is extended by 4 pixels (green edge) and the lipid content C_{L} in the defined region is fitted using the function

$$
\begin{aligned}
l(x,y) &= \frac{C}{2}\left(1+\mathrm{erf}\left(\frac{R-r_\epsilon}{\sigma}\right)\right), \text{ with} \qquad (1)\\
r_\epsilon &= \sqrt{(\epsilon((x-x_0)\cos\theta-(y-y_0)\sin\theta))^2+(\epsilon^{-1}((x-x_0)\sin\theta-(y-y_0)\cos\theta))^2},
\end{aligned}
$$

where C is the peak concentration in the LD, R is the effective radius of the droplet, (x_0, y_0) is the center position, ϵ is the LD ellipticity, θ is the angle of the major axis relative to the x direction, and σ is the width of the edges,

Fig. S14(b,d) shows the obtained fit of the lipid content in the droplets with the red

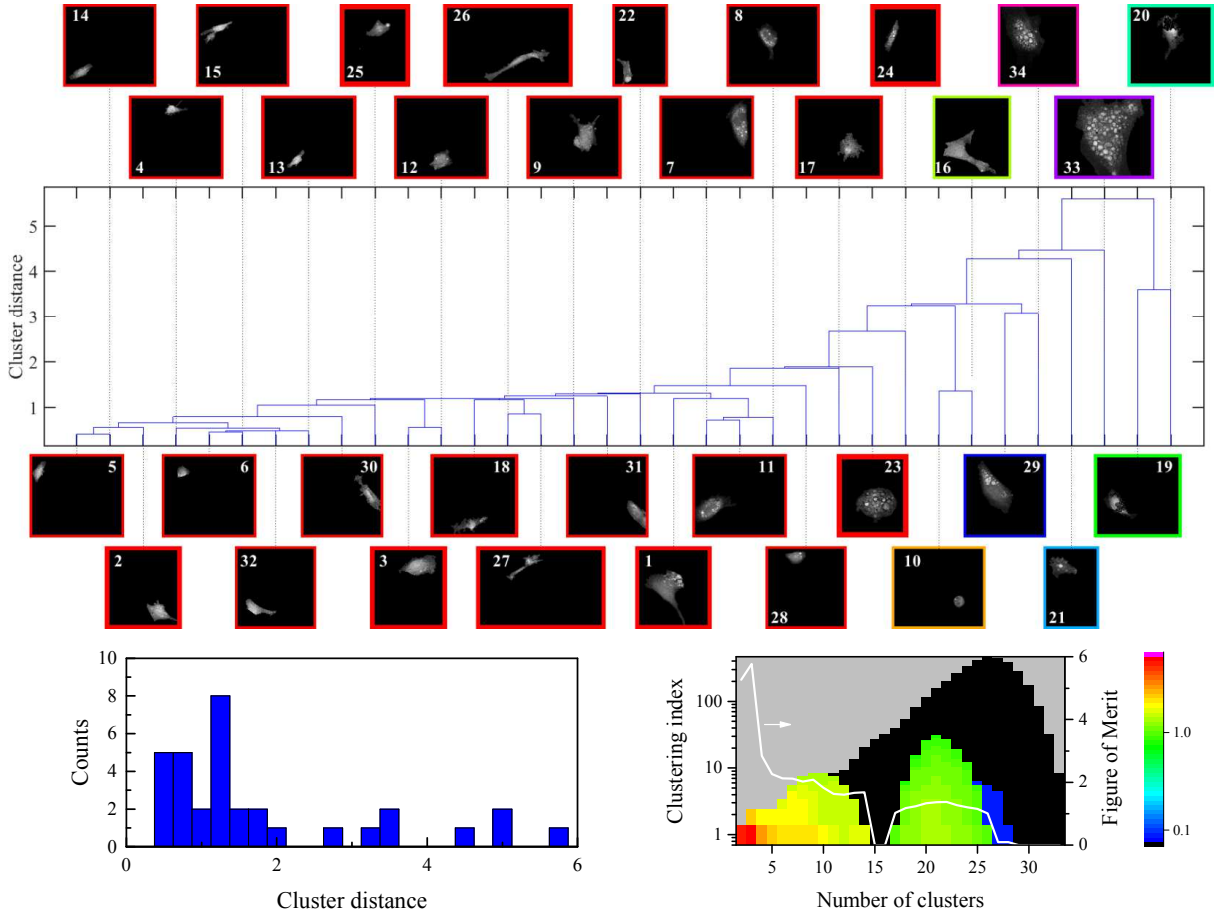

FIG. S13: Same as Fig. 3 when 7 PCs are included in the HCA.

crosses indicating the position of the centroid.

For each droplet, we then analysed the distribution of the protein concentration around the LD as sketched in Fig. 4. We evaluated the mean value of the protein concentration by integrating the concentration over the contour of the quadrant $s(r)$ of radius r centred at $\mathbf{r}_0$. The direction $\mathbf{d}$ of the quadrant was determined by the average direction of the protein concentration from $\mathbf{r}_0$ as the line integral

$$\mathbf{d} = \oint_{s_c(r)} C_P(\mathbf{r})\mathbf{r}\, dl \tag{2}$$

over the full circle $s_c(r)$ for the smallest $r > R$ for which the maximum is larger than 10%, to identify the protein rich vesicles. We then evaluated the mean protein concentration $\bar{C}_P(r)$ and its standard deviation $\hat{C}_P(r)$ as the line integrals:

$$\bar{C}_P(r) = \oint_{s(r)} C_P(\mathbf{r})\, dl \Big/ \oint_{s(r)} dl\ , \tag{3}$$

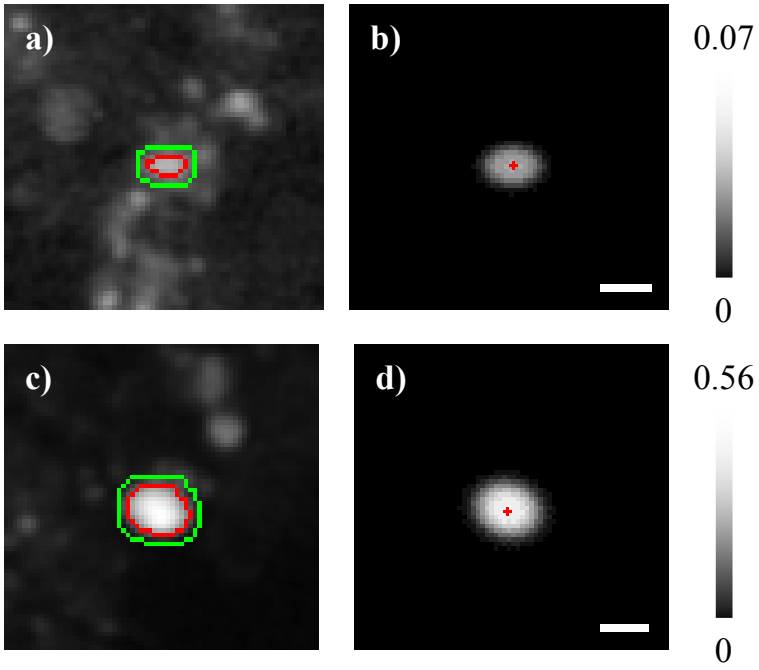

FIG. S14: a),c): Lipid concentration distribution C_{L} for the areas shown in Fig. S15 and Fig. 4, respectively. The red pixels identify the edge of the mask obtained by the segmentation procedure. The green pixels represent the edges of the mask after extension. The maximum lipid concentration for each grayscale are given on the side. b),d): Simulated lipid concentration obtained by the fit of the lipid content within the green edges using the function discussed in the text. The red crosses indicate the position (x_0, y_0) of the obtained centroids. The images have the same grayscale as a) and c), respectively. The scale bar indicates 5 μm.

$$\hat{C}_{\mathrm{P}}(r) = \sqrt{\oint_{s(r)} \left(\frac{C_{\mathrm{P}}(\mathbf{r})}{\bar{C}_{\mathrm{P}}(r)} - 1 \right)^2 dl \Big/ \oint_{s(r)} dl}\,, \tag{4}$$

In these calculations we included only the pixels where $C_{\mathrm{L}} < 10\%$ and $C_{\mathrm{S}} > 5\%$, to exclude regions outside the cell or inside lipid droplets.

S10. CALCULATION OF THE PROTEIN CONCENTRATION AROUND A LIPID DROPLET USING THE FULL CIRCULAR CONTOUR

Fig. S15 shows the results for the protein concentrations around the lipid droplets calculated as described in the main manuscript, but using a full circular contour instead of a direction quadrant.

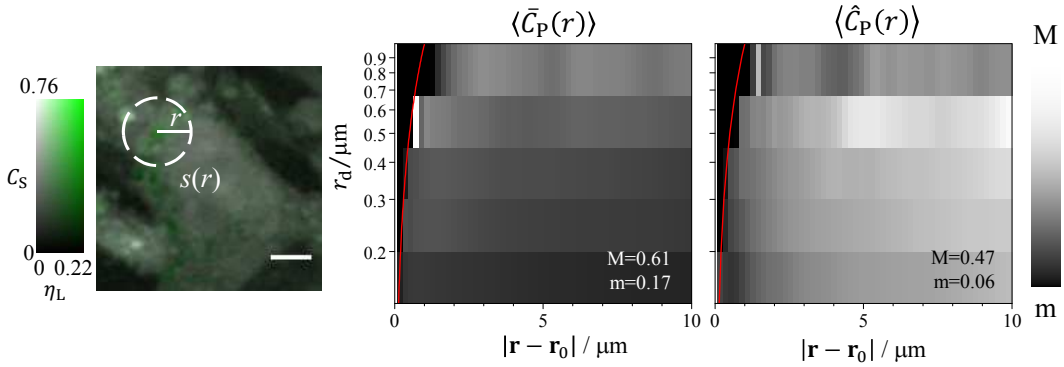

FIG. S15: Left: Sketch of the integration contours used to calculate $\bar{C}_P(r)$ and $\hat{C}_P(r)$ around the lipid droplets, with the full circle $s(r)$. The image is a zoom of the areas indicated in Fig. 1(b). The colour scale is shown on the left, with the brightness proportional to C_S and the saturation of the green hue proportional to η_L, with saturation of 1 corresponding to η_L= 0.22. The scale bar represents 5 μm. Center and right: Radial distribution of the protein concentration $\langle \bar{C}_P(r) \rangle$ (center) and its relative standard deviation $\langle \hat{C}_P(r) \rangle$ (right) around LDs as function of the effective LD radius r_d. The red lines show $r_d = |\mathbf{r} - \mathbf{r}_0|$. Linear grayscale as in Fig. 4.

Acknowledgments

We thank Elisabetta Canetta for the spontaneous Raman measurements

---

* Electronic address: masiaf@cf.ac.uk

[1] Cardiff University data archive: http://dx.doi.org/10.17035/d.2017.0009096459.

[2] Z. Yu, T. Chen, X. Zhang, D. Fu, X. Liao, J. Shen, X. Liu, B. Zhang, X. S. Xie, X.-D. Su, et al., Chem. Sci. **3**, 2646 (2012).

[3] C. Di Napoli, I. Pope, F. Masia, W. Langbein, P. Watson, and P. Borri, Anal. Chem. **88**, 3677–3685 (2016).

[4] M. Troyanova-Wood, C. Gobbell, Z. Meng, A. A. Gashev, and V. V. Yakovlev, J. Biophotonics **1**, 9 (2017).

[5] D. Moseti, A. Regassa, and W.-K. Kim, Int. J. Mol. Sci. **17**, 124 (2016).

[6] For the minimization we used the Matlab function fminsearchbnd developed by John D'Errico. The code of the function can be found at

http://www.mathworks.com/matlabcentral/fileexchange/8277-fminsearchbnd–fminsearchcon or requested to the authors.

[7] P. Rousseeuw, J. Comput. Appl. Math. **20**, 53 (1987).